Editor's Choice

Dry and hydrated defective molybdenum Disulfide/Graphene bilayer heterojunction under strain for hydrogen evolution from water Splitting: A First-principle study

Nicholas Dimakis [a],[*], Sanju Gupta [b], Razeen Wadud [a], Muhammad I. Bhatti [a]

[a] *Department of Physics and Astronomy, University of Texas Rio Grande Valley, Edinburg 78539, USA*
[b] *Department of Materials Science and Engineering, Pennsylvania State University, University Park 16802, USA*

A B S T R A C T

In search of exploiting cost-effective, highly stable, efficient, and greatly active electrocatalysts for hydrogen evolution reaction (HER), molybdenum disulfide-graphene heterostructures (MoS_2/graphene) are promising, in contrast to noble metals. We used density functional theory (DFT) to examine the changes in the electronic structure of MoS_2/graphene under compressive strain for structural defects in the MoS_2 and graphene layers, as well as from hydration of the MoS_2 layer. In the pristine MoS_2/graphene heterostructure, a small bandgap (minigap) is opened at the graphene Dirac point, which is located above the Fermi energy, for dry and hydrated configurations. The presence of sulfur and carbon vacancies in the MoS_2/graphene upshifts the Dirac point and widens the minigap. However, additional sulfur vacancies further widen or shrink the minigap depending on the location of the MoS_2 conduction band bottom and the presence of defect bands at the Dirac point. The minigap tunability in the MoS_2/graphene heterostructure could be engineered for producing efficient HER electrocatalysts and beyond. The Quantum Theory of Atoms in Molecules (QTAIM) reveals S—C bond critical points, which correspond to van der Waals forces interactions in agreement with the Non-covalent Interaction (NCI) analysis. A correlation is drawn between the minigap and the electron density at the S—C bond critical points.

1. Introduction

Growing electrical energy demand in daily life associated with rapid consumption of conventional fossil fuels has pressed for exploring alternative clean and sustainable energy sources. In general, green energy industry uses energy produced from various renewable sources including solar, wind, geothermal, and water electrolysis [1]. The environmentally friendly electrochemical water splitting (EWS) has been widely researched as an advanced energy conversion technology to produce clean and renewable hydrogen (H_2) fuel, by coupling with other renewable energy sources, such as the solar-driven photoelectrochemical (PEC) approach [2]. Hydrogen extraction requires the use of an efficient hydrogen evolution reaction (HER) catalyst, such as platinum and palladium-based alloys [3–5]. However, these precious metals are expensive and leads to poisoning, which calls for ongoing search for earth-abundant and inexpensive alternative electrocatalysts beyond noble metals. Therefore, despite numerous advantages, the practical application of hydrogen production by EWS method has been greatly hindered by the limitations of highly efficient electrocatalysts and photocatalysts (i.e., photo-assisted electrocatalyst).

In the quest of promising electrocatalysts and photocatalysts, transition metal dichalcogenides (TMDs) and transition metal phosphides (TMPs) have attracted broad interests owing to their abundant merits including natural abundance, high electron conductivity, promising catalytic activity, and stability [6,7]. Molybdenum disulfide (MoS_2) is a classic two-dimensional layered material within the family of TMDs, which among its other uses, such as serving as an optoelectronic device [8,9], it can be also used as an HER catalyst of high efficiency [10] thus, replacing expensive noble metal-based alloys. The MoS_2 monolayer can be extracted from the MoS_2 bulk via mechanical exfoliation [11,12] or from flakes [13]. The MoS_2 monolayer, in its trigonal prismatic (2H) configuration (2H-MoS_2), is a direct bandgap semiconductor of 1.8 eV [14]. It has several favorable properties relevant for HER due to the presence of sulfurized or sulfur containing (S) electroactive sites on Mo edges [15] and at intrinsic point defects (or extrinsic created by either electrochemical desulfurization or low power oxygen plasma) associated with sulfur [16] or occasionally Mo atoms [17]. The presence of S defects introduces defect states within the band structure and thus, midgaps in the energy region around the Fermi energy for the 2H-MoS_2. Li et al. found that as hydrogen is adsorbed on the S defect site, its Gibbs

---

free energy is lowered due to the presence of the defect states, thus assisting H₂ release [18]. Therefore, electronic band structure and molecular "orbital engineering" of electrode surfaces under electrochemical environment or electrified interfaces could be used to select the appropriate 2H-MoS₂ defect configuration for a high efficiency 2H-MoS₂ HER catalyst. The strain of the MoS₂ basal plane further enhances the MoS₂ catalytic efficiency, by altering the MoS₂ band structure and electron density distribution [19].

The defect-free basal planes of 2D layers are catalytically inactive [20]. However, catalytic activity on the formerly inert basal planes has been reported for the MoS₂ monolayer and reduced graphene oxide (rGO) heterostructure [20]. Biroju et al. showed that pristine graphene on top of a few layered stacked MoS₂ van der Waals heterostructure exhibited higher catalytic activity compared to the activity of individual layers or other stacked heterostructure configurations [21].

The "stacking sequence" that leads to the optimal HER heterostructures is not completely understood yet. Biroju et al. explored the "stacking sequence" for pristine MoS₂ monolayers and graphene using density functional theory (DFT) and found that placing graphene on top of a pristine MoS₂ monolayer leads to the highest photoresponse and the lowest charge-transfer resistance toward HER [22]. Additionally, the electrocatalytic activity of the MoS₂ can be enhanced by increasing its conductivity through the addition of a defective graphene layer underneath [16]. The combination of the chemically inert graphene with MoS₂ in a single electrode as heterostructure provides better electron conduction and ion transportation, thus offering new opportunities and rationales to improve the performance of energy devices. The MoS₂/graphene heterostructure is also found in a variety of applications, such as electronic logic and memory devices [23], photodetectors [24,25], spintronics [26], and energy storage devices [27]. These heterostructures can be fabricated by the bottom-up chemical vapor deposition of MoS₂ on a graphene or dry transfer methods [28]. The electronic band structure of the MoS₂/graphene heterostructure shows the presence of a small bandgap (minigap-ΔE) at the graphene Dirac point (E_D), due to the hybridization of the graphene C-p_z bands with the Mo-d conduction band bottom [29]. Electronic structure methods based on DFT combine numerical efficiency with satisfactory accuracy, while predicting electrode behavior at the most fundamental level, which helps in designing the electrodes for electrocatalysis. In this work, we use extensive DFT calculations to examine the effects of S and C vacancies and hydration, while simulating the electrochemical environment on the electronic band structure of the MoS₂/graphene heterostructure. Specifically, we will examine how the Dirac point shifts due to vacancies and hydration are correlated with the width of minigap in the vicinity of the Dirac point. Moreover, we use Quantum Theory of Atoms in Molecules (QTAIM) [30,31] and Non-covalent Interaction (NCI) analyses to elucidate the MoS₂/graphene behavior in dry and hydrated conditions [32].The MoS₂/graphene heterostructure is both an electrocatalyst and photocatalyst since MoS₂ can absorb light in the visible region [21].

2. Computational methods

2.1. Structure modeling and charge redistributions

The pristine dry MoS₂/graphene heterostructure under comprehensive strain is constructed by a 2H-MoS₂ three-layer 4 × 4 lattice of 48 atoms, with S atoms occupying the top and bottom layers and Mo atoms residing in the middle layer, overlayered on a 3 $\sqrt{3}$× 3 $\sqrt{3}R30°$ monolayer graphene (54 atoms). Fig. 1a, b show the unit cell of the pristine MoS₂/graphene heterostructure, which contains 102 atoms. This supercell arrangement allows for lattice mismatch within the MoS₂ and graphene, as expected by the presence of strain [29]. In our past work, we found that the interlayer spacings for all of these structures were between 3.13 and 3.17 Å [17], in agreement with Klimeš et. al., who used a 3:4 supercell arraignment [33]. The presence of strain is verified

(a)

(b)

(c)

$d_{Mo-S} = 2.35$ Å
$d_{C-C} = 1.40$ Å
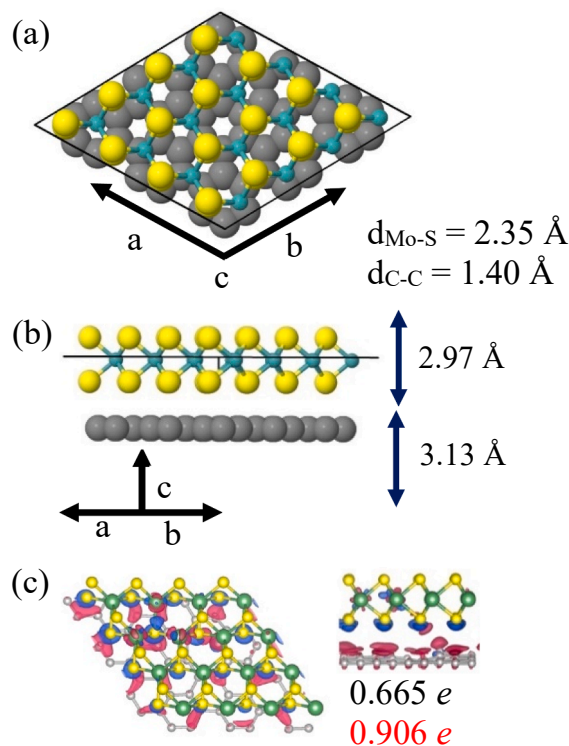
2.97 Å

3.13 Å

0.665 e
0.906 e

Fig. 1. The DFT optimized dry pristine MoS₂/graphene unit cell using the PBE0 functional, as shown from two different orientations (a) side and (b) top. The thick black lines are the unit cell boundaries. Atoms are colored as follows: S, yellow; Mo, green; C: gray. Visualization is via Jmol. (c) Charge redistributions $\Delta \rho(\vec{r})$ for MoS₂/graphene with a single S and C vacancy per unit cell. Blue and magenta isospheres correspond to areas of charge accumulation and depletion, respectively. Maxima isodensity surfaces of 0.001 e/bohr³ are displayed. Black and red values refer to charge transferred per unit cell from graphene towards MoS₂, using Mulliken and iterative Hirshfeld populations, respectively. (For interpretation of the references to colour in this figure legend, the reader is referred to the web version of this article.)

by the charge transfer from graphene to MoS₂ (Fig. 1c) for all MoS₂/graphene configurations in this work (Fig. S1, S2, Supplementary Material). Defective MoS₂/graphene heterostructures are built by considering all combinations of single (V_S) and non-adjacent double S vacancies (V_{S2}) in the MoS₂ with a single C vacancy (V_C) in the graphene layer. Hydrated MoS₂ surfaces contain the equivalent of three water molecules per unit cell (i.e., 0.1875 ML coverage; waters are placed on S layer away from graphene).

Fig. 1c shows the charge redistributions for due to hydration $\Delta \rho(\vec{r})$ defined as

$$\Delta\rho(\vec{r}) = \rho_{MoS_2/graphene}(\vec{r}) - \rho_{MoS_2}(\vec{r}) - \rho_{graphene}(\vec{r}) \tag{1}$$

where $\rho_{MoS_2/graphene}(\vec{r})$, $\rho_{MoS_2}(\vec{r})$, and $\rho_{graphene}(\vec{r})$ are the charge density distributions in real space of the dry MoS₂/graphene and the isolated MoS₂ and graphene, respectively. The $\Delta \rho(\vec{r})$ remaining configurations of this work can be found in the supplementary materials (Fig. S1 and S2). For hydrated configurations, Eq. (1) is expanded to include the additional term of $-\rho_{waters}(\vec{r})$.

The hydrogen adsorption energy $E_{ads}(H)$ is calculated as

$$E_{ads}(H) = E(MoS_2/graphene\text{-}H) - E(MoS_2/graphene) - \frac{1}{2}E(H_2) \tag{2}$$

where $E(MoS_2/graphene\text{-}H)$ and $E(MoS_2/graphene)$ are the total energies for the heterostructure with and without adsorbed H, respectively and $E(H_2)$ is the energy of the free H₂. The Gibbs free energy ΔG_H for the adsorbed hydrogen is given by

$$\Delta G_H = E_{ads}(\text{H}) + \Delta G_{ZPE} - T\Delta S_H \qquad (3)$$

where ΔG_{ZPE} and ΔS_H are the zero-point energy (ZPE) and entropy difference between the adsorbed and the gas phase states, respectively. The sum of these two terms is about 0.24 eV [34]. Thus,

$$\Delta G_H \cong E_{ads}(\text{H}) + 0.24\text{eV} \qquad (4)$$

2.2. DFT parameters

The CRYSTAL17 [35] code is used to calculate the electronic properties for dry and hydrated MoS$_2$/graphene heterostructures with and without vacancies. The advantage of CRYSTAL is its treatment on two-dimensional slabs without the need of artificial periodicity perpendicular to the surface, which is typically found in other DFT codes [36]. We use two DFT functionals here: The PBE0 non-empirical/parameter-free functional [37,38] and the HSE06 screened hybrid functional of Heyd, Scuseria, and Ernzerhof, which provides band gaps in better agreement with experimental findings [39]. The use of two functionals allow us to examine if the electronic structures calculations results are systematic.

All calculations are treated using the D3 semiempirical correction by Grimme [40], which improves the DFT functionals descriptions of the long-range electron correlations responsible for van der Waals interactions. The S, C, O, and H atoms are described by all-electron basis sets, which are optimized for crystalline calculations, whereas effective core potentials (ECP) are used for Mo atoms [41]. A 24 × 24 grid is used for densities of states (DOS) and the electronic band structures calculations. The following path was used: M-Γ-K-M-Γ, with M (1/2, 0, 0), Γ (0, 0, 0), and K (1/3, 1/3, 0). Here, the Γ point of the supercell Brillouin zone (BZ) coincides with the K point of the unit cell BZ, and the E_D is found at the Γ point of the supercell BZ.

2.3. QTAIM and NCI parameters

QTAIM provides information about the bonding type and strength between two atoms through the studies of topologies for the electron density ($\rho(\vec{r})$) and its Laplacian ($\nabla^2\rho(\vec{r})$). The presence of a bond critical point is a necessary condition for bonding between two atoms. The bond critical points are linked with the corresponding nuclei via
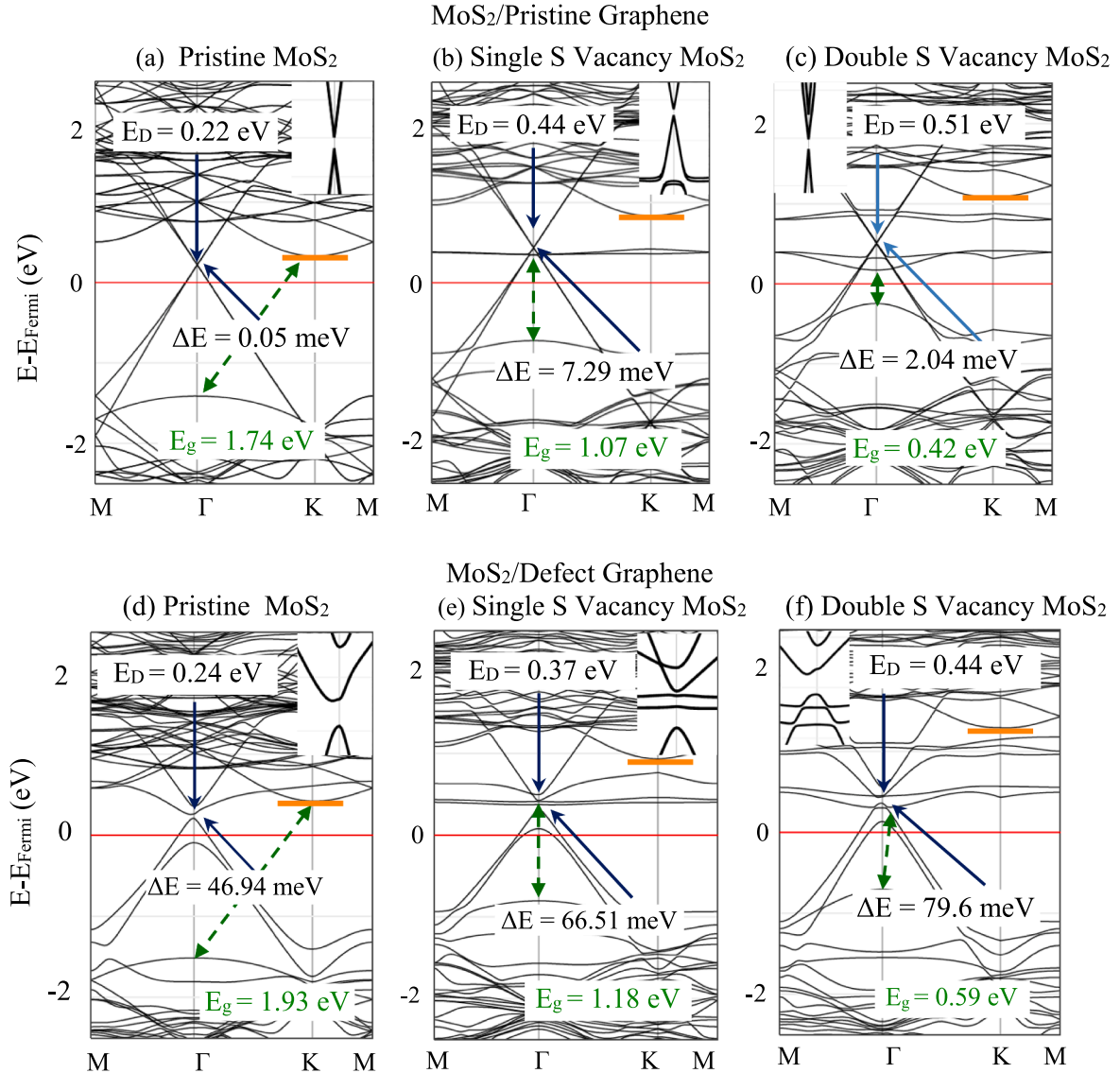

Fig. 2. Band structures for dry MoS$_2$/graphene with and without S and C vacancies. Red solid horizontal lines are Fermi energies. Dashed green arrows show the MoS$_2$ bandgaps and mid-gaps (E_g; bandgaps, (a) and (d); mid-gaps (b), (c), (e), and (f)). Minigaps (ΔE) and approximate Dirac points (E_D) are shown with blue arrows. Values refer to HSE06 calculations. Inserts show the gap in the area around the E_D. Orange horizontal bars show the MoS$_2$ conduction band bottom. (For interpretation of the references to colour in this figure legend, the reader is referred to the web version of this article.)

paths. The collection of these paths is the molecular graph [42]. In this work, we use QTAIM to examine the bond critical points, which appear between the S layer of the MoS$_2$ and graphene (i.e., S—C bond critical points). QTAIM analyses are basis set and method independent, as long as a minimally adequate basis set is used [43]. The $\rho(\vec{r})$ topology is performed by the Multiwfn [44] program through the GAMESS program output [45] on a cluster extracted from the periodic layer. The NCI method is used to study weak interactions via calculation of the reduced density gradient (RDG) parameter ($\propto \frac{|\nabla\rho(\vec{r})|}{\rho(\vec{r})^{4/3}}$) and plotting of the RDG map. QTAIM $\rho(\vec{r})$ at bond critical points and bandgaps have been correlated previously [46].

3. Results and discussion

3.1. Electronic structure analysis

Figs. 2 and 3 show the band structure for all MoS$_2$/graphene

configurations of this work for the HSE06 calculations. The corresponding PBE0 calculations can be found in the electronic supplementary material (Fig. S3 and S4). The calculated band structure with the PBE0 functional provides larger MoS$_2$ bandgaps relative to the HSE06 calculations, as expected [47]. However, we also observed some minor changes in the band structure around the Dirac point between these two calculations and are related to the location of the defect states (vide infra). Fig. 4 shows the densities of states calculations (DOS) for the dry configurations of this work, whereas the hydrated counterparts can be found in the supplementary material (Fig. S5).

3.1.1. Dry pristine MoS$_2$/graphene heterostructures

We begin our analysis by examining the changes in the graphene electronic structure due to the presence of the MoS$_2$ monolayer, when both MoS$_2$ and graphene are pristine and dry. In the pristine MoS$_2$/graphene case, the Dirac point appears above the Fermi energy (E_F) at about 0.22 eV and 0.14 eV for HSE and PBE0 calculations, respectively and these upshifts are due to the MoS$_2$ and graphene lattice mismatches.
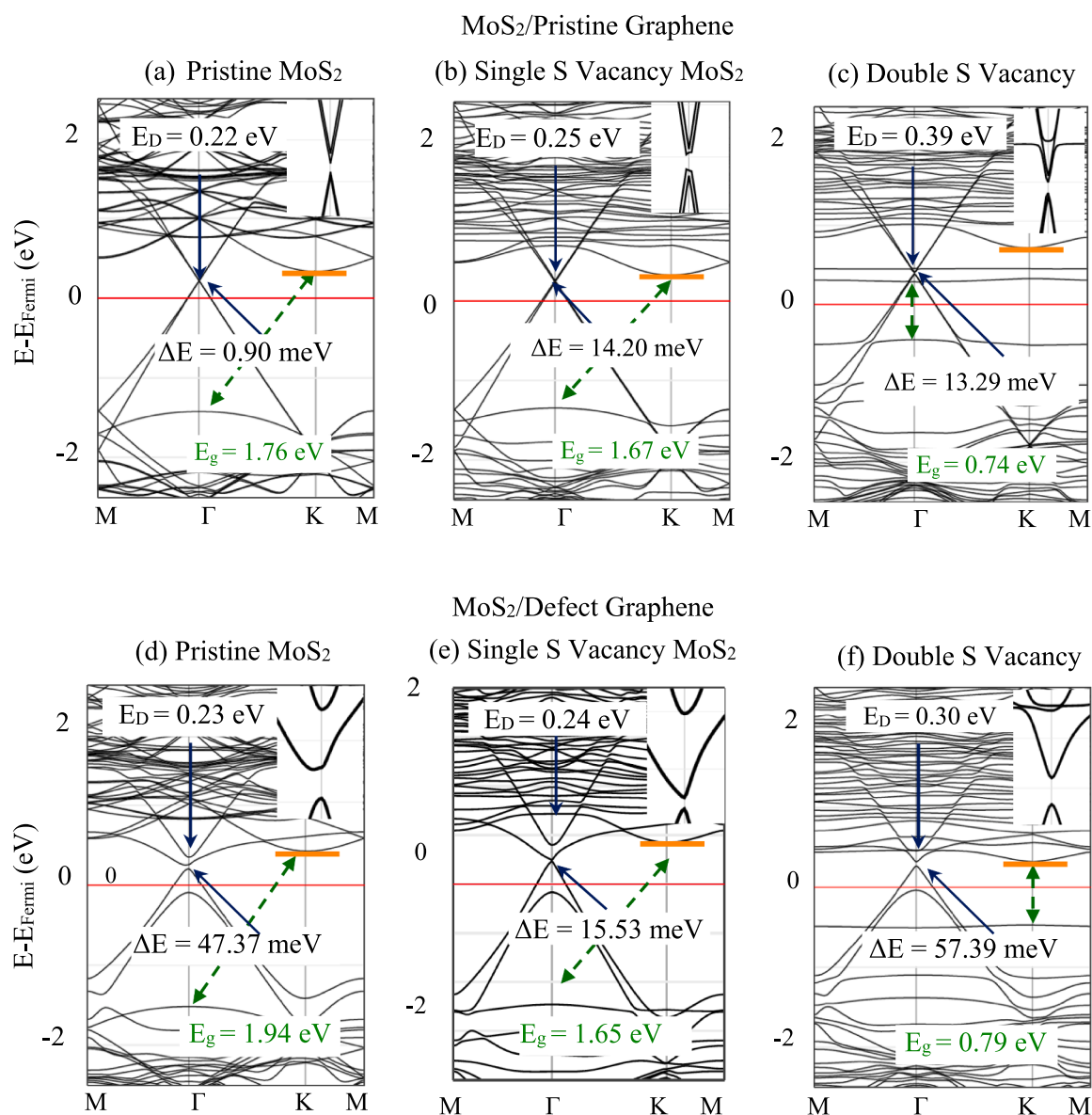

Fig. 3. Band structures for hydrated MoS$_2$/graphene with and without S and C vacancies. Red solid horizontal lines are Fermi energies. Dashed green arrows show the MoS$_2$ bandgaps and mid-gaps (E_g; bandgaps, (a) and (d); mid-gaps (b), (c), (e), and (f)). Minigaps (ΔE) and approximate Dirac points (E_D) are shown with blue arrows. Values refer to HSE06 calculations. Inserts show the gap in the area around the E_D. Orange horizontal bars show the MoS$_2$ conduction band bottom. (For interpretation of the references to colour in this figure legend, the reader is referred to the web version of this article.)
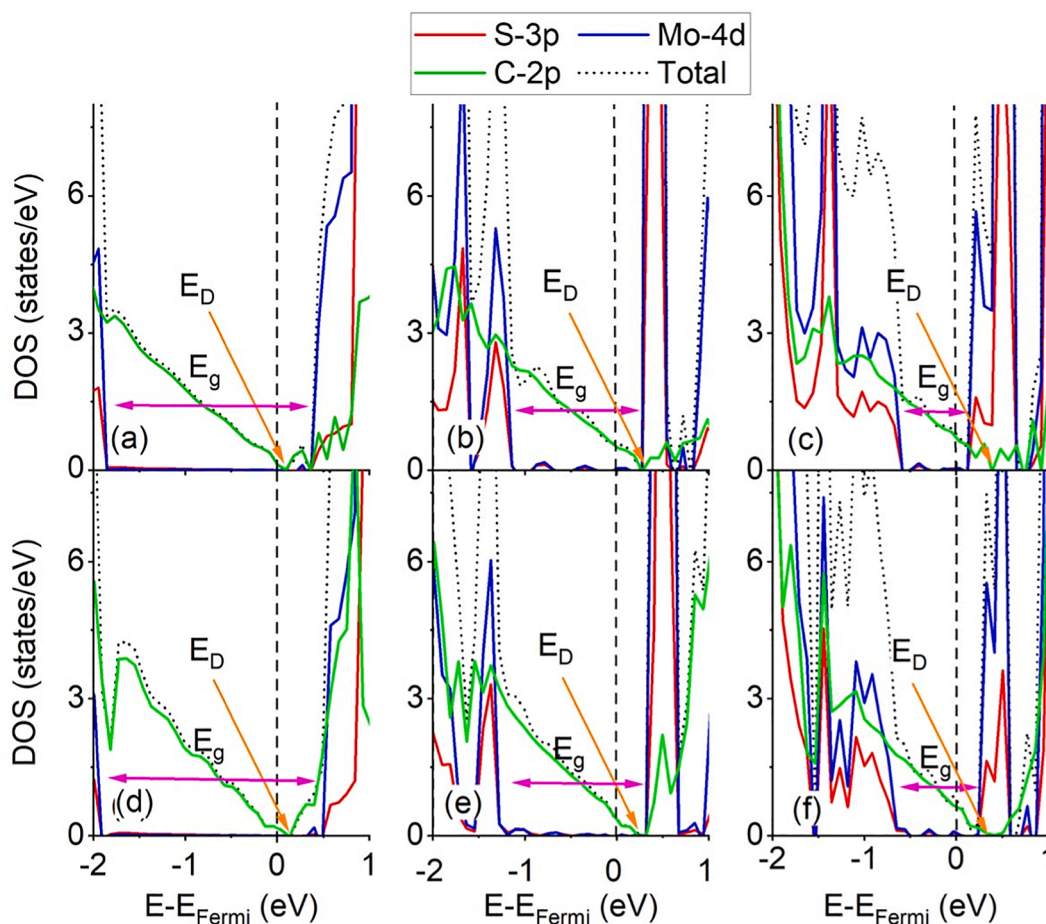
Fig. 4. DOS for dry MoS_2/graphene with and without S and C vacancies under the PBE0 calculations. Dashed vertical lines are Fermi energies. Dirac points (E_D) are shown. (a) Pristine, (b) V_S, (c) V_{S2}, (c) V_C, (d) V_C and V_S, and (e) V_C and V_{S2}.

The observed minigaps in the vicinity of the E_D (see Figs. 2 and 3 and Figs. S3 and S4) are of the order of meV, for all configurations in this work (<1 meV for pristine MoS_2/graphene). The DOS show that for pristine MoS_2/graphene the top of its valance band contains S-3p and Mo-4d orbitals, whereas in the MoS_2 conduction band bottom the Mo-d dominates, in a similar fashion as for the corresponding bands of the isolated 2H-MoS_2 case (Fig. 4, S5). For all dry configurations of this work, the MoS_2 conduction band bottom upshifts along with the V_S increases (Fig. 2, S2). Additional calculations show that for the dry pristine case, the highest occupied crystalline orbital (HOCO) at the Γ point of the supercell BZ is C-p_z and the lowest unoccupied crystalline orbital (LUCO) is Mo-d_{xy} and $d_{x^2-y^2}$. The presence of graphene also alters the MoS_2 electronic structure by changing the MoS_2 bandgap from direct in the isolated 2H-MoS_2 to indirect, in agreement with previous reports [29].

3.1.2. Dry defect MoS_2/graphene heterostructures

We now turn our focus for the case of MoS_2/graphene heterostructure with V_S and V_{S2} at the S layer away from the graphene layer. The presence of V_S and V_{S2} introduce defect bands in the MoS_2/graphene band structure and in turn mid-gaps (i.e., energy gaps between defect states). There is an inverse relationship between the MoS_2 mid-gaps and the number of S vacancies for both dry and hydrated configurations. The band structure calculations show that MoS_2 mid-gaps appear at their lowest values for the heterostructure configurations under V_{S2} (Figs. 2 and 3, Figs. S3, S4). Similar information is revealed by the DOS calculations (Fig. S5).

In the V_S case, for dry MoS_2, additional almost flat degenerate defect

bands appear in the vicinity of the Dirac point, whereas in the V_{S2} case defect bands appear above and below the Dirac point. We found that all defect configurations have larger minigaps than their pristine counterparts due to C-p_z hybridization with Mo-d defect states (flat bands). However, increased S vacancies do not always lead to larger minigaps. Moreover, for defect configurations shorter distances between MoS_2 and graphene do not always increase the minigap, in a sticking contrast with past reports, which refer to pristine monolayers [29]. For example, comparing dry MoS_2/graphene between V_S and V_{S2} we found that the minigap is decreased as the number of S vacancies are increasing, concomitant with the decrease of the MoS_2-graphene distance. This is due to the weaker mixing of the C-p_z with the MoS_2 defect states, which contain d orbitals of Mo atoms around the defect, since in the V_{S2} case, these states are more distant in energy from the E_D relative to the V_S case (Fig. 2, S2). The C defect causes a bandgap opening at the E_D, which is also observed for isolated graphene. Thus, the dry heterostructures with C vacancies have minigaps that are substantially larger than their pristine counterparts and this statement also applies to the hydrated cases except for the hydrated V_{S2} configuration under the PBE0 calculation (Fig. S4f).

3.1.3. Hydrated MoS_2/graphene heterostructures

The interaction of water molecules with pristine MoS_2 is weak [48], whereas water is dissociated, when is adsorbed at S defect locations [47]. Specifically, the hydration effect on defect MoS_2 is associated with one out of three waters in the unit cell to be dissociated at the vacancy site, leading to strong OH adsorption on the Mo site. Hydration slightly decreases the charge transfer between MoS_2 and graphene (Fig. S2) and

this effect alone decreases the C-p_z and Mo-d overlap. For the hydrated configurations, the conduction band bottom is slightly downshifted in energy between pristine MoS$_2$ and V$_S$ configurations, whereas it upshifts for V$_{S2}$ (Fig. 3, S4,). This is in contrast with the systematic upshift of the MoS$_2$ conduction band bottom observed for the dry configurations. Hydration of pristine MoS$_2$ monolayer causes a minor upshift of the Mo conduction band bottom, leading to a small increase in the MoS$_2$ bandgap (Fig. 2a, Fig. 3a). This is due to increased C-p_z and Mo-d hybridization, which in turn, widens the minigap.

For the hydrated configurations under pristine graphene, the minigaps widen along with increased V$_S$. This is explained as follows: The hydrated V$_S$ configuration has a slightly downshifted conduction band bottom relative to the pristine counterpart, which increases the C-p_z and Mo-d hybridization. As the S vacancies increase the conduction band bottom upshifts and defect states appear at the Dirac point area. Therefore, changes in the minigaps are due to the location of the conduction band bottom and the presence of defect bands in the Dirac point. Interestingly, some of the minigaps have values above k_BT (~40 meV at T = 300 °K), and thus, could transform the electronic character from metallic to a semiconductor-like heterostructure.

3.2. MoS$_2$/graphene as an HER catalyst

The MoS$_2$/graphene heterostructure can be evaluated as an HER catalysts via calculation of the adsorbed H Gibbs free energy ΔG_H using Eqs. (2)–(4). Optimally, $\Delta G_H \cong 0 eV$. We performed additional DFT calculations using the PBE0 functional to obtain optimal geometries for H adsorbed on MoS$_2$ and on graphene, using the MoS$_2$/graphene dry configurations. In the case that both MoS$_2$ and graphene are pristine, hydrogen is found in the center of the MoS$_2$ hexagone for H/MoS$_2$ and adsorbed atop on C for H/graphene, in agreement with past reports [22]. Specifically, the shortest S—H distance and the C—H distance are 1.42 Å and 1.12 Å, respectively for H adsorption on the pristine MoS$_2$/graphene surfaces. When S defects are present on MoS$_2$, H is in the center of the Mo triangle around the S vacancy, in a similar fashion as in the hydrated MoS$_2$/graphene cases, where one of the water molecules is dissociated in the vacancy S site. Hydrogen adsorption at the S vacancy sites is stronger than adsorption on pristine MoS$_2$. Fig. 5 shows ΔG_H for H adsorption on MoS$_2$ and graphene, where for both cases, we observe positive and negative ΔG_H values. For H/MoS$_2$, ΔG_H is positive, when MoS$_2$ is pristine and negative elsewhere. Specifically, there is an analogous relationship between ΔG_H being more negative and the number of S vacancies (Fig. 5a).

For H/graphene, when C vacancies are present, H is absorbed at the vacancy site. Hydrogen is adsorbed strongly on C with C—H = 1.07 Å and the C-H appears tilted relative to the graphene plane for MoS$_2$/graphene configurations with V$_C$ and V$_C$ and V$_{S2}$. This leads to ΔG_H = −2.57 eV for either case. However, for MoS$_2$/graphene with V$_C$ and V$_S$, C—H = 1.1 Å, the adsorption is atop as in the pristine cases and ΔG_H = −0.52 eV, which is significantly less negative than the other two cases examined above.

We will now explain how the ΔG_H can be used to select the optimal MoS$_2$/graphene configuration as HER catalyst. In the pristine case, ΔG_H are 1.89 eV and 0.83 eV for H adsorbed on MoS$_2$ and graphene, respectively. Thus, for this case, H adsorption on graphene is preferred than on MoS$_2$, in agreement with Biroju et al. [22]. However, the presence of S vacancies changes ΔG_H from positive to negative. Thus, a selection of S vacancies concentration can be used to obtain ΔG_H close to 0 eV, for H/MoS$_2$. This technique has been applied by Tsai et al. for selecting the optimal S concentration for 2H-MoS$_2$ [49].

3.3. QTAIM and NCI analysis

QTAIM analysis revealed several S—C bond critical points with low electron density values $\rho(\vec{r})$ at the order of 10^{-2} a.u. Table 1 shows the average values of the $\rho(\vec{r})$ and $\nabla^2\rho(\vec{r})$ at the S—C bond critical points and the distances from these bond critical points to the S layer of the MoS$_2$ and graphene for the PBE0 calculations. We were not able to obtain convergence for the hydrated MoS$_2$/graphene under V$_{S2}$ and V$_C$ and V$_{S2}$. There is an analogous relationship between changes in the $\rho(\vec{r})$ and $\nabla^2\rho(\vec{r})$ for all configurations examined in this section with the exception of the dry and hydrated V$_C$ and V$_S$ configurations. The presence of S vacancies slightly decreases the distance between MoS$_2$ and graphene. However, this change of the distance is not correlated with changes in the minigap. Table 1 shows that for the configurations examined here, the Laplacian is positive and at same order of 10^{-2} a.u. as the electron density. This suggests that S-C bonding is of a closed shell
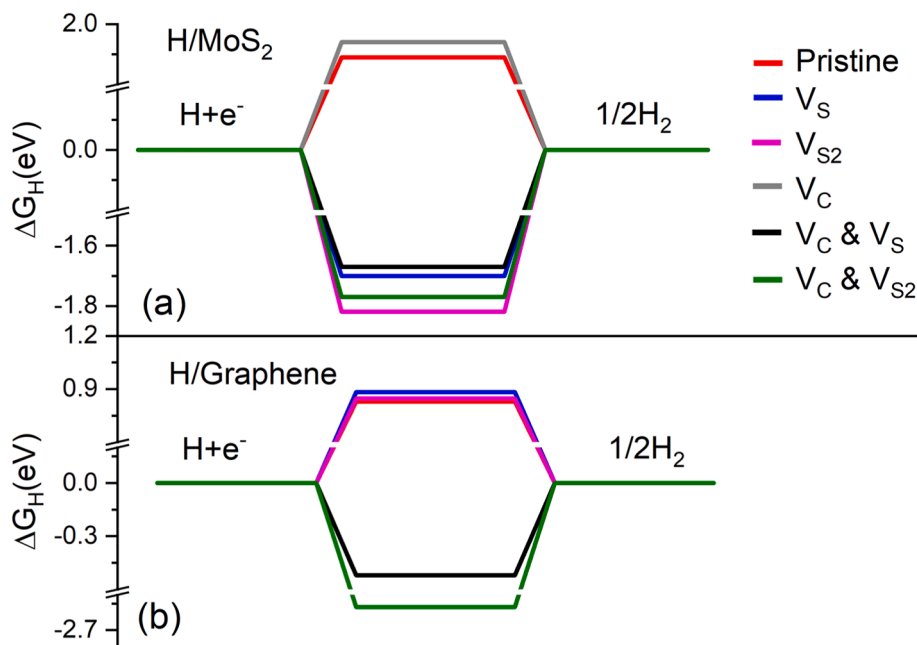

Fig. 5. Plot of ΔG_H for H adsorption on (a) MoS$_2$ and (b) graphene for each MoS$_2$/graphene configuration. For H adsorption on graphene the ΔG_H for V$_C$ and V$_C$ & V$_{S2}$ configurations are about the same.

Table 1

Multiwfn calculated average values of the QTAIM parameters $\rho(\vec{r}_{bcp})$ and $\nabla^2\rho(\vec{r}_{bcp})$ and distances from the S—C bond critical points (bcp) to the S layer of the MoS_2 and graphene for the PBE0 calculations. Values in parathesis refer to the corresponding hydrated cases.

Configuration	QTAIM parameters			
	$\rho(\vec{r}_{bcp})$ $(\times 10^{-2} a.u.)$	$\nabla^2\rho(\vec{r}_{bcp})$	d_{MoS_2-bcp} (Å)	$d_{bcp-graphene}$
Pristine	1.11	4.32	1.73	1.41
	(1.15)	(4.42)	(1.73)	(1.41)
V_S	1.18	4.52	1.72	1.40
	(1.08)	(4.15)	(1.73)	(1.41)
V_{S2}	1.18	4.49	1.71	1.40
V_C	1.07	4.10	1.74	1.43
	(1.09)	(4.21)	(1.73)	(1.43)
V_C & V_S	1.30	4.67	1.67	1.49
	(1.15)	(4.25)	(1.82)	(1.44)
V_C & V_{S2}	1.24	4.48	1.67	1.49

[50]. The presence of these bond critical points explains why the heterostructure is stable.

Fig. 6 shows the molecular graph for the dry pristine MoS_2/graphene with NCI *iso*-surfaces and the average $\rho(\vec{r})_{S-C}$ vs. ΔE for dry configurations. The NCI *iso*-surfaces in the vicinity of the S—C points denote

that the S-C interactions are van der Waals, whereas steric interactions appear at the center of the graphene rings. We must state that QTAIM analysis alone cannot specify if the closed shell S—C bonding is van der Waals and this is achieved by the using information from the NCI analysis. Fig. 5c shows a correlation between the electron density at the S—C bond critical points and the minigap at the Dirac point. Wider minigaps of about 60 mV and higher appear for the dry and the hydrated configurations with V_C and V_S and the dry configuration with V_C and V_{S2}, the latter being the widest.

We also showed that the MoS_2/graphene minigap at the Dirac point is correlated with the presence of S and C vacancies and hydration.

4. Conclusions

In this work, we showed that the MoS_2/graphene minigap at the Dirac point is correlated with the presence of S and C vacancies and hydration. Specifically, the presence of S and C vacancies increase the minigap, whereas increased S vacancies do not always widen it. Importantly, opening or closing of the minigap depends on the locations of the MoS_2 conduction band and the defect states at the Dirac point. Hydration increases the MoS_2/graphene minigap, when graphene is pristine, whereas when graphene is defective no clear trend is observed. An optimal HER MoS_2/graphene catalyst could be engineered by selecting the S vacancy concentrations with ΔG_H close to 0 eV. QTAIM and NCI analyses displayed that the S—C bonding is van der Waals and
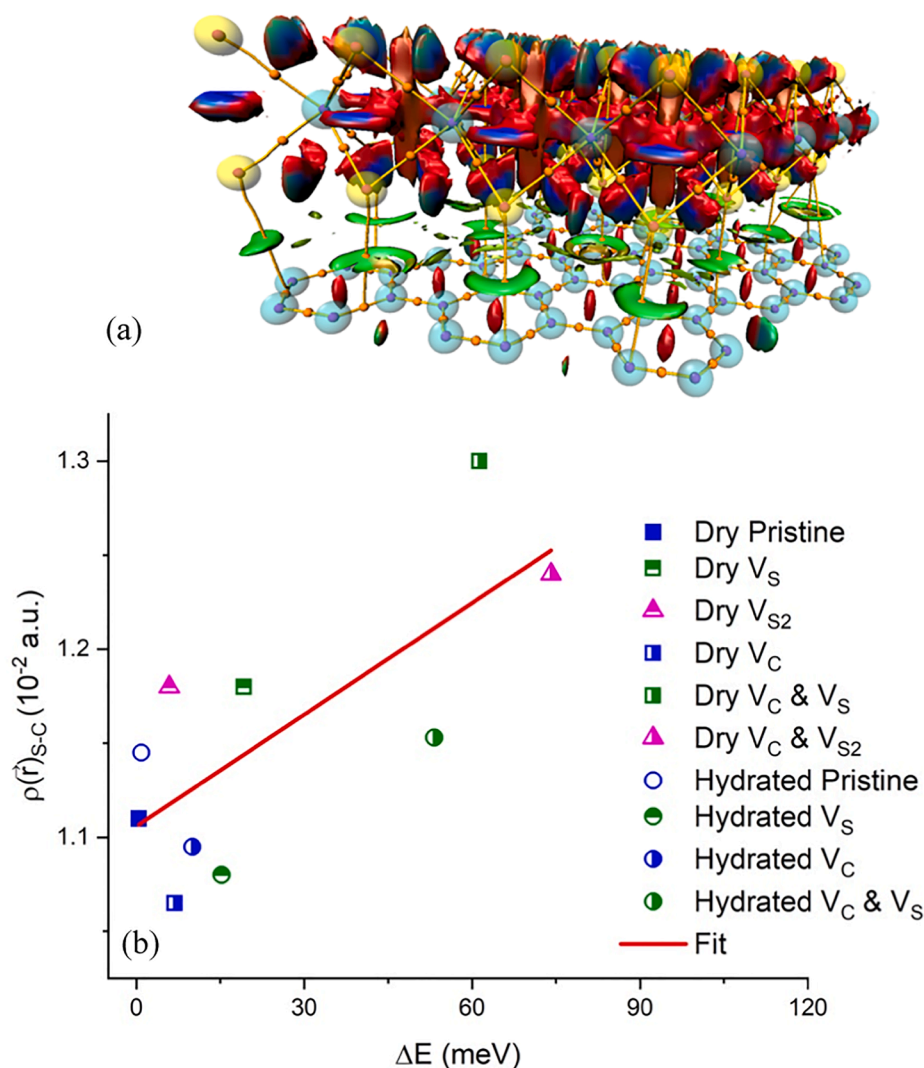

(a)

Fig. 6. (a) QTAIM molecular graphs and NCI iso-surfaces obtained from the DFT optimized unit cell for dry MoS_2/graphene using Multiwfn and plotted via VMD [51]. Small and large spheres denote critical points and atoms, respectively. Atoms colors are as follows: S, yellow; Mo, green; C, carbon. QTAIM critical points are colors as follows: nuclear critical points purple; bond critical points, orange. Surface colors are as follows: Green: van den Waals; red, repulsion; blue, attraction. (b) $\rho(\vec{r})_{S-C}$ vs. ΔE for PBE0 calculations. (For interpretation of the references to colour in this figure legend, the reader is referred to the web version of this article.)

(b)

the average electron density at these points is correlated with the minigap. Thus, the QTAIM analysis can serve as local density probe to describe bond-breaking or bond-making processes directly relevant for HER related electrocatalytic processes, making the design of emerging electrocatalysts practically feasible expected to lie at the summit of the Sabatier plot (so-called volcano plot).

CRediT authorship contribution statement

Nicholas Dimakis: Conceptualization, Methodology, Supervision, Validation, Writing – review & editing. **Sanju Gupta:** Conceptualization, Methodology, Writing – review & editing. **Razeen Wadud:** Visualization, Investigation, Validation. **Muhammad I. Bhatti:** Writing – review & editing.

Declaration of Competing Interest

The authors declare that they have no known competing financial interests or personal relationships that could have appeared to influence the work reported in this paper.

Appendix A. Supplementary material

Supplementary data to this article can be found online at https://doi.org/10.1016/j.commatsci.2022.111234.

Reference

[1] J.A. Turner, Sustainable Hydrogen Production, Science 305 (2004) 972–974.

[2] X. Li, X. Yang, H. Xue, H. Pang, Q. Xu, Metal–organic frameworks as a platform for clean energy applications, EnergyChem 2 (2020), 100027.

[3] N. Cheng, S. Stambula, D. Wang, M.N. Banis, J. Liu, A. Riese, B. Xiao, R. Li, T.-K. Sham, L.-M. Liu, G.A. Botton, X. Sun, Platinum single-atom and cluster catalysis of the hydrogen evolution reaction, Nat. Commun. 7 (2016) 13638.

[4] R. Subbaraman, D. Tripkovic, D. Strmcnik, K.-C. Chang, M. Uchimura, A. P. Paulikas, V. Stamenkovic, N.M. Markovic, Enhancing Hydrogen Evolution Activity in Water Splitting by Tailoring Li$^+$-Ni(OH)$_2$-Pt Interfaces, Science 334 (2011) 1256–1260.

[5] R.-Q. Yao, Y.-T. Zhou, H. Shi, Q.-H. Zhang, L. Gu, Z. Wen, X.-Y. Lang, Q. Jiang, Nanoporous Palladium-Silver Surface Alloys as Efficient and pH-Universal Catalysts for the Hydrogen Evolution Reaction, ACS Energy Lett. 4 (2019) 1379–1386.

[6] T. Zhang, J. Du, P. Xi, C. Xu, Hybrids of Cobalt/Iron Phosphides Derived from Bimetal-Organic Frameworks as Highly Efficient Electrocatalysts for Oxygen Evolution Reaction, ACS Appl. Mater. Interfaces 9 (2017) 362–370.

[7] L. Yan, L. Cao, P. Dai, X. Gu, D. Liu, L. Li, Y. Wang, X. Zhao, Metal-Organic Frameworks Derived Nanotube of Nickel-Cobalt Bimetal Phosphides as Highly Efficient Electrocatalysts for Overall Water Splitting, Adv. Funct. Mater. 27 (2017) 1703455.

[8] S. Kim, A. Konar, W.-S. Hwang, J.H. Lee, J. Lee, J. Yang, C. Jung, H. Kim, J.-B. Yoo, J.-Y. Choi, Y.W. Jin, S.Y. Lee, D. Jena, W. Choi, K. Kim, High-mobility and low-power thin-film transistors based on multilayer MoS2 crystals, Nat. Commun. 3 (2012) 1011.

[9] O. Lopez-Sanchez, D. Lembke, M. Kayci, A. Radenovic, A. Kis, Ultrasensitive photodetectors based on monolayer MoS2, Nat. Nanotechnol. 8 (2013) 497–501.

[10] R.S. Trasatti, Work function, electronegativity, and electrochemical behaviour of metals: III. Electrolytic hydrogen evolution in acid solutions, J. Electroanal. Chem. 39 (1972) 163–184.

[11] K.S. Novoselov, D. Jiang, F. Schedin, T.J. Booth, V.V. Khotkevich, S.V. Morozov, A. K. Geim, Two-dimensional atomic crystals, Proc. Natl. Acad. Sci. U. S. A. 102 (2005) 10451–10453.

[12] H.S.S. Ramakrishna Matte, A. Gomathi, A.K. Manna, D.J. Late, R. Datta, S.K. Pati, C.N.R. Rao, MoS2 and WS2 analogues of graphene, Angew. Chem. Int. Edit. 49 (2010) 4059–4062.

[13] J. Zhang, T. Wang, D. Pohl, B. Rellinghaus, R. Dong, S. Liu, X. Zhuang, X. Feng, Interface Engineering of MoS2/Ni3S2 Heterostructures for Highly Enhanced Electrochemical Overall-Water-Splitting Activity, Angew. Chem. Int. Edit. 55 (2016) 6702–6707.

[14] K.F. Mak, C. Lee, J. Hone, J. Shan, T.F. Heinz, Atomically Thin MoS$_2$: A New Direct-Gap Semiconductor, Phys. Rev. Lett. 105 (2010) 136805–1136804.

[15] T.F. Jaramillo, K.P. Jørgensen, J. Bonde, J.H. Nielsen, S. Horch, I. Chorkendorff, Identification of Active Edge Sites for Electrochemical H$_2$ Evolution from MoS$_2$ Nanocatalysts, Science 317 (2007) 100–102.

[16] Y. Cheng, H. Song, H. Wu, P. Zhang, Z. Tang, S. Lu, Defects Enhance the Electrocatalytic Hydrogen Evolution Properties of MoS$_2$-based Materials, Chem. Asian J. 15 (2020) 3123–3134.

[17] S. Gupta, T. Robinson, N. Dimakis, Electrochemically Desulfurized Molybdenum Disulfifide (MoS2) and Reduced Graphene Oxide Aerogel Composites as Efficient Electrocatalysts for Hydrogen Evolution, J. Nanosci. Nanotechnol. 20 (2020) 6191–6214.

[18] J. Li, J. Kang, Q. Cai, W. Hong, C. Jian, W. Liu, K. Banerjee, Boosting Hydrogen Evolution Performance of MoS2 by Band Structure Engineering, Adv. Mater. Interfaces 4 (2017) 1700303.

[19] H. Peelaers, C.G. Van de Walle, Effects of strain on band structure and effective masses in MoS$_2$, Phys. Rev. B 86 (2012), 241401.

[20] H. Li, K. Yu, C. Li, Z. Tang, B. Guo, X. Lei, H. Fu, Z. Zhu, Charge-Transfer Induced High Efficient Hydrogen Evolution of MoS2/graphene Cocatalyst, Sci. Rep. 5 (2015) 18730.

[21] R.K. Biroju, S. Pal, R. Sharma, P.K. Giri, T.N. Narayanan, Stacking sequence dependent photo-electrocatalytic performance of CVD grown MoS2/graphene van der Waals solids, Nanotechnology 28 (2017), 085101.

[22] R.K. Biroju, D. Das, R. Sharma, S. Pal, L.P.L. Mawlong, K. Bhorkar, P.K. Giri, A. K. Singh, T.N. Narayanan, Hydrogen Evolution Reaction Activity of Graphene–MoS2 van der Waals Heterostructures, ACS Energy Lett. 2 (2017) 1355–1361.

[23] S. Bertolazzi, D. Krasnozhon, A. Kis, Nonvolatile Memory Cells Based on MoS2/Graphene Heterostructures, ACS Nano 7 (2013) 3246–3252.

[24] K.Y. Thai, I. Park, B.J. Kim, A.T. Hoang, Y. Na, C.U. Park, Y. Chae, J.-H. Ahn, MoS2/Graphene Photodetector Array with Strain-Modulated Photoresponse up to the Near-Infrared Regime, ACS Nano 15 (2021) 12836–12846.

[25] W. Zhang, C.-P. Chuu, J.-K. Huang, C.-H. Chen, M.-L. Tsai, Y.-H. Chang, C.-T. Liang, Y.-Z. Chen, Y.-L. Chueh, J.-H. He, M.-Y. Chou, L.-J. Li, Ultrahigh-Gain Photodetectors Based on Atomically Thin Graphene-MoS2 Heterostructures, Sci Rep-Uk 4 (2014) 3826.

[26] I. Žutić, J. Fabian, S. Das Sarma, Spintronics, Fundamentals and applications, Rev. Modern Phys. 76 (2004) 323–410.

[27] H. Wang, D. Tran, J. Qian, F. Ding, D. Losic, MoS2/Graphene Composites as Promising Materials for Energy Storage and Conversion Applications, Adv. Mater. Interfaces 6 (2019) 1900915.

[28] Y. Shi, W. Zhou, A.-Y. Lu, W. Fang, Y.-H. Lee, A.L. Hsu, S.M. Kim, K.K. Kim, H. Y. Yang, L.-J. Li, J.-C. Idrobo, J. Kong, van der Waals Epitaxy of MoS2 Layers Using Graphene As Growth Templates, Nano Lett. 12 (2012) 2784–2791.

[29] S. Singh, C. Espejo, A.H. Romero, First-principles investigation of graphene/MoS$_2$ bilayer heterostructures using Tkatchenko-Sche er van der Waals method, Phys. Rev. B 98 (2018) 155309–155310.

[30] R.F.W. Bader, Atoms in Molecules, in: Encyclopedia of Computational Chemistry, John Wiley and Sons, 1998.

[31] R. Bader, Atoms in Molecules: A Quantum Theory, Oxford Univ. Press, in, Oxford, 1990.

[32] E.R. Johnson, S. Keinan, P. Mori-Sánchez, J. Contreras-García, A.J. Cohen, W. Yang, Revealing Noncovalent Interactions, J. Am. Chem. Soc. 132 (2010) 6498–6506.

[33] J. Klimeš, D.R. Bowler, A. Michaelides, Van der Waals density functionals applied to solids, Phys. Rev. B 83 (2011), 195131.

[34] J.K. Nørskov, T. Bligaard, A. Logadottir, J.R. Kitchin, J.G. Chen, S. Pandelov, U. Stimming, Trends in the Exchange Current for Hydrogen Evolution, J. Electrochem. Soc. 152 (2005) J23.

[35] R. Dovesi, V.R. Saunders, C. Roetti, C.M. Zicovich-Wilson, F. Pascale, B. Civalleri, K. Doll, N.M. Harrison, I.J. Bush, P. D'Arco, M. Llunell, M. Causà, Y. Noël, L. Maschio, R. Orlando, A. Erba, M. Rérat, S. Casassa, CRYSTAL17 User's Manual, Univ. Torino, Torino, 2017.

[36] H. Shi, R. Eglitis, G. Borstel, Ab initio calculations of the BaF$_2$ bulk and surface F centres, J. Phys.: Condens. Matter 18 (2006) 8367.

[37] M. Ernzerhof, G.E. Scuseria, Assessment of the Perdew–Burke–Ernzerhof exchange-correlation functional, J. Chem. Phys. 110 (1999) 5029–5036.

[38] C. Adamo, V. Barone, Toward reliable density functional methods without adjustable parameters: The PBE0 model, J. Chem. Phys. 110 (1999) 6158–6170.

[39] A.V. Krukau, O.A. Vydrov, A.F. Izmaylov, G.E. Scuseria, Influence of the exchange screening parameter on the performance of screened hybrid functionals, J. Chem. Phys. 125 (2006) 224106–1224105.

[40] S. Grimme, J. Antony, S. Ehrlich, H. Krieg, A consistent and accurate ab initio parametrization of density functional dispersion correction (DFT-D) for the 94 elements H-Pu, J. Chem. Phys. 132 (2010) 154104–154118.

[41] J. Laun, D.V. Oliveira, T. Bredow, Consistent gaussian basis sets of double- and triple-zeta valence with polarization quality of the fifth period for solid-state calculations, J. Comput. Chem. 39 (2018) 1285–1290.

[42] P.L.A. Popelier, On the full topology of the Laplacian of the electron density, Coord. Chem. Rev. 197 (2000) 169–189.

[43] M. Jabłoński, M. Palusiak, Basis set and method dependence in atoms in molecules calculations, J. Phys. Chem. A 114 (2010) 2240–2244.

[44] T. Lu, F. Chen, Multiwfn: A multifunctional wavefunction analyzer, J. Comput. Chem. 33 (2012) 580–592.

[45] M.W. Schmidt, K.K. Baldridge, J.A. Boatz, S.T. Elbert, M.S. Gordon, J.H. Jensen, S. Koseki, N. Matsunaga, K.A. Nguyen, S. Su, T.L. Windus, M. Dupuis, J. A. Montgomery, General Atomic and Molecular Electronic Structure System, J. Comput. Chem. 14 (1993) 1347–1363.

[46] M.A. Syzgantseva, O.A. Syzgantseva, QTAIM method for accelerated prediction of band gaps in perovskites, Theor. Chem. Acc 138 (2019) 52–58.

[47] N. Dimakis, O. Vadodaria, K. Ruiz, S. Gupta, Molybdenum disulfide monolayer electronic structure information as explored using density functional theory and quantum theory of atoms in molecules, Appl. Surf. Sci. 149545 (2021).

[48] B. Zhao, C. Shang, N. Qi, Z.Y. Chen, Z.Q. Chen, Stability of defects in monolayer MoS$_2$ and their interaction with O$_2$ molecule: A first-principles study, Appl. Surf. Sci. 412 (2017) 385–393.

[49] C. Tsai, H. Li, S. Park, J. Park, H.S. Han, J.K. Nørskov, X. Zheng, F. Abild-Pedersen, Electrochemical generation of sulfur vacancies in the basal plane of MoS2 for hydrogen evolution, Nat. Commun. 8 (2017) 15113.

[50] C. Gatti, Chemical bonding in crystals: new directions, Z. Kristallogr. Cryst. Mater. 220 (2005) 399–457.

[51] W. Humphrey, A. Dalke, K. Schulten, VMD - Visual Molecular Dynamics, J. Molec. Graphics 14 (1996).